Energy Storage Materials 24 (2020) 682–688

Contents lists available at ScienceDirect

Energy Storage Materials

journal homepage: www.elsevier.com/locate/ensm

Converting a thick electrode into vertically aligned "Thin electrodes" by 3D-Printing for designing thickness independent Li-S cathode

Xuejie Gao [a,b,1], Xiaofei Yang [a,1], Qian Sun [a], Jing Luo [a], Jianneng Liang [a], Weihan Li [a,b], Jiwei Wang [a,b], Sizhe Wang [a], Minsi Li [a,b], Ruying Li [a], Tsun-Kong Sham [b,**], Xueliang Sun [a,*]

[a] Department of Mechanical and Materials Engineering, University of Western Ontario, London, Ontario, N6A 5B9, Canada
[b] Department of Chemistry, University of Western Ontario, London, Ontario, N6A 5B7, Canada

ARTICLE INFO

Keywords:
Thickness independent cathode
High sulfur loading
Vertically-aligned thin electrode
3D printing
Lithium sulfur battery

ABSTRACT

Sulfur cathodes with a high sulfur loading more than 3 mg cm^{-2} are essential for practical high-energy density Li-S batteries. However, Li^+ transport is usually poor in thick cathodes, resulting in low capacity output, fast capacity decay and large overpotential. To tackle the issue of thick sulfur cathodes, a thickness-independent electrode structure is proposed for the first time which can transform a thick electrode into a combination of vertically aligned "thin electrodes". Each "thin electrode" has a thickness of ~20 μm, which is independent of the overall thickness of electrode or sulfur loading. The "thin electrodes" substantially enhanced local accessibility to Li^+ and e^- and enabled similar electrochemical kinetics in spite of the total sulfur loading or thickness of the electrode. Accordingly, highly similar cycling performance and rate performance were demonstrated with the 250 μm and 750 μm (i.e. sulfur loadings of 2 and 6 mg cm^{-2}) electrodes. This work demonstrates the concept and offers a new opportunity for designing high-loading cathodes and shall rise interests for other energy storage systems such as Li-ion batteries, Li-air batteries, etc.

1. Introduction

Lithium–sulfur (Li-S) batteries have been considered as one of the most perspective candidates of future batteries due to their superior theoretical energy density of 2600 Wh kg^{-1} and low cost, naturally abundant, and environmental friendly of sulfur [1–6]. Nevertheless, there are still intricate challenges, such as low Li^+/e^- conductivity of sulfur and Li_2S/Li_2S_2, large volumetric changes during cycling, and the widely known "shuttle effects", remaining to be solved [7–10]. These problems lead to low Coulombic efficiency, low sulfur utilization, fast capacity fading and poor cycle life, which hinder the practical application of Li-S batteries [7,9,11,12]. Recently, tremendous efforts have been focused on suppressing polysulfides (PSs) shuttling between anode and cathode via physical confinement and chemical absorption [13]. Based on these attempts, good cycling performance of Li-S batteries up to 1000 cycles have been achieved [14,15]. Despite the significant achievements, it should be noted that most of these long cycle lives were demonstrated with low sulfur loading cathodes less than 2 mg cm^{-2} [16].

To achieve high energy density, high sulfur loading and high active material utilization are essential. Nonetheless, a high sulfur loading is usually accompanied by an increase in electrode thickness [17,18]. The electrochemical performance of Li-S batteries can be highly affected by the cathode thickness as a result of the prolonged and tortuous ion transport. What is worse, the high concentration of Li_2S formed on the cathode surface further hindered the Li^+ and PS diffusion inside the cathode, resulting in incomplete electrochemical reaction and low sulfur utilization [19,20]. To tackle these issues, construction of Li^+ transporting channels in the cathode is a favorable strategy [9,21–24]. For instance, Zhang and coworkers developed a "tri-continuous phase" porous electrodes, achieving a capacity of around 800 mAh g^{-1} for the 7 mg cm^{-2} sulfur-loaded electrode [21]. Further avoiding the shrinkage of the Li^+ transport channels under surface tension via a freeze-drying method, a 24 mg cm^{-2} sulfur-loaded electrode was successfully demonstrated at 0.05 C [21]. However, even with this progress, the increase of electrode thickness and sulfur loading still cause low capacity output, large overpotential, and poor cycling stability and rate performance.

* Corresponding author.
** Corresponding author.
E-mail address: xsun9@uwo.ca (X. Sun).
[1] These authors contributed equally to this work.

https://doi.org/10.1016/j.ensm.2019.08.001
Received 6 May 2019; Received in revised form 1 August 2019; Accepted 2 August 2019
Available online 6 August 2019

Generally, the electrochemical performance of the reported Li-S batteries is still highly dependent on cathode thicknesses. Recently, our group demonstrated that the Li^+ transport in Li-S cathode could be optimized from macroscale and nanoscale via 3D printing method, but it still suffers from capacity decay with increased S loading [25]. Impressively, Yang and co-workers developed a vertically aligned two-dimensional titanium carbide ($Ti_3C_2T_x$) electrode for supercapacitors. Beneficial from the fast Li^+ transport in the vertical-aligned channels and reduced Li^+ transport distance, the supercapacitors assembled with 40-μm and 200-μm electrodes exhibited almost the same rate performance [26]. However, such thickness-independent properties have never been reported in Li-S battery systems in spite of great efforts focused on vertical-aligned electrodes based on graphene nanowalls, [27] carbon nanosheets, [28] and graphite flakes [29].

Herein, a thickness-independent electrode with high sulfur loading Li-S cathode was proposed, for the first time, to convert the 3D disordered thick electrode into a combination of numerous vertically aligned 2D "thin electrodes" by integrating the 3D-printing technology with an ice-template method. In our previous work, it has demonstrated that 3D printing technology can ensure high active material loading with a thick electrode for batteries [30]. Therefore, in this work, employing the ice as a vertically-aligned template can successfully transform the thick electrodes into numerous "thin electrodes". Each "thin electrode" presents a constant thickness of around 20 μm. The "thin electrodes" are independent of the total thickness of printed electrodes, even if the total electrode thickness can be scaled up to hundreds of microns using 3D printing. It is widely known that the electrochemical reaction can only occur at the tri-phase interface with active materials, Li^+ source (electrolyte), and e^- source (active electrode surface). Each individual "thin electrode" functions as an electrochemical reaction site, with a Li^+ diffusion distance no more than 10 μm considering a bi-directional transport model and neglecting the tortuosity within the "thin electrodes". The Li^+ transporting resistance can be significantly reduced compared to the traditional dense electrodes with several hundred micro-meters. Additionally, the "thin electrodes" are beneficial for alleviating Li_2S_2/Li_2S blockage as well. The similar electrochemical kinetics, Li^+/e^- conductivities, and constant local thickness in "thin electrodes" make it possible to achieve thickness-independent electrochemical performance of electrodes. Consistently, highly similar cycling performance and rate performance are observed for 3D-printed vertically aligned electrodes, no matter total thickness of 250 or 750 μm (i.e. sulfur loadings of 2 mg cm^{-2} and 6 mg cm^{-2}). Both electrodes deliver a capacity of 530 mAh g^{-1} at 10 mA cm^{-2} and a low capacity decay of 0.1% per cycle over 200 cycles at 1 mA cm^{-2}.

2. Experimental section

2.1. Synthesis of S/BP-2000 composite

600 mg of sulfur powder (99.5%, Sigma-Aldrich) was mixed with 400 mg conductive carbon (Cabot BP-2000) with a weight ratio of 6:4 by grinding with a mortar and a pestle for 0.5 h. The mixture was transferred into a sealed steel reactor and heated at 155 °C for 8 h and subsequently 300 °C for 4 h. After cooling to room temperature, the final S/BP-2000 composite with a sulfur content of 60 wt % was obtained.

2.2. Fabrication of 3DP-VAEs and 3DP-NVAEs

3DP-VAEs and 3DP-NVAEs with different sulfur loadings were fabricated using a custom-made 3D printer equipped with a 3-axis micro-positioning stage (FFF Delta 3D printer) motorized by stepper motors (CNC4PC, CS4EA4-1Rev1). S/BP-2000 composite, Na alginate, and acetylene black were mixed at a weight ratio of 7:1.5:1.5 with additional DI water to prepare the printing ink. The ink was loaded into a 3-mL syringe and extruded through a 250-μm-diameter nozzle. The 3DP-VAEs and 3DP-NVAEs were printed into a grid structure with an overall diameter of 10 mm at a print motion speed of 6 mm s^{-1}. The printed electrodes were dried using two different methods for comparison: 1) freeze-drying at −50 °C for 20 h (namely 3DP-VAEs with sulfur loading of 2 mg cm^{-2} and 6 mg cm^{-2}) and 2) thermal drying in a vacuum oven at 60 °C for 20 h (3DE-NVAEs with sulfur loading of 2 mg cm^{-2} and 6 mg cm^{-2}).

2.3. Characterizations

Hitachi S-4800 field-emission scanning electron microscope (FESEM) equipped with energy dispersive spectroscopy (EDS) was used to characterize the morphologies of the printed samples. The sulfur content in the S/BP 2000 composite was determined by an SDT Q600 thermogravimetric analyzer (TGA) under a nitrogen atmosphere from room temperature to 600 °C with a heating rate of 10 °C min^{-1}.

2.4. Electrochemical measurements

The electrochemical performance of the 3DP-VAEs and 3DP-NVAEs with different sulfur loadings were assembled with CR2032 coin cells in an Ar-filled glovebox. The cathode and Li anode were separated by a polypropylene membrane (Celgard 2400). The electrolyte in this study was 1 M bis (trifluoromethylsulfonyl) imide (LiTFSI) in 1, 2-dimethoxymethane (DME)/1, 3-dioxolane (DOL) (1:1 v/v) with 1 wt % $LiNO_3$ additive. The electrolyte/sulfur (E/S) ratio is controlled as around 10 μL mg^{-1} for both 3DP-VAEs and 3DP-NVAEs.The cycling performance of the assembled batteries were tested using a LAND battery testing station, by applying different current. Electrochemical impedance spectroscopy (EIS) was tested at open-circuit with a frequency range of 5.0×10^5 Hz to 1.0×10^{-2} Hz on a versatile multichannel potentiostation 3/Z (VMP3). Cyclic voltammetry (CV) was performed on the same instrument and the data was collected under a scanning rate of 0.1 mV s^{-1} between a voltage of 1.8 V and 2.8 V. The charge-discharge tests were carried out using a LAND CT-2001A system with voltages between 1.8 V and 2.8 V at room temperature. Unless otherwise specified, the specific capacities reported in this work were calculated based on sulfur and the voltages vs. Li^+/Li.

3. Results and discussion

Fig. 1 schematically presents the fabrication and application of a 3D-printed vertical aligned electrode (3DP-VAE). There are three main steps in to the fabrication process. Firstly, the cathode ink was prepared by dispersing S/BP 2000 composite, acetylene black conductive additives, sodium alginate in a weight ratio of 14:3:3 in an aqueous solution. Subsequently, the ink was printed into a round grid pattern with 1 cm diameter using a 3D printer. It should be noted that the total thickness and areal sulfur loading of electrode can be easily controlled by adjusting the number of printing layers. Lastly, the as-printed electrode was freeze-dried to obtain the 3DP-VAE as a cathode for Li-S batteries.

The formation mechanism and the morphology of 3DP-VAE are shown in Fig. 2. Ice, the solid phase of water, has been widely used as a template for synthesizing porous materials, especially porous ceramics [31]. As shown in Fig. 2a, according to the basic crystallographic and the anisotropic crystal growth kinetics, the ice growth rate along structure does not the a-axis is 10^2 to 10^3 times higher than that along the b-axis, thereby forming lamellar walls of ice. The aligned ice walls act as templates to divide the thick electrode into numerous "thin electrodes". After the removal of the ice-templates by freeze-drying, a 3DP-VAE with vertically aligned "thin electrodes" is fabricated [32]. The optical images of 3DP-VAE-6 (sulfur loading of 6 mg cm^{-2}) before and after freeze drying in Fig. S1, show an obvious printed grid structure with three layers. The free-standing structure do not require additional current collectors. The microscopic morphologies are characterized by scanning electron microscopy (SEM). As shown in Fig. 2b, the printed grid electrode was composed of interwoven fibers with a diameter of 250 μm. The

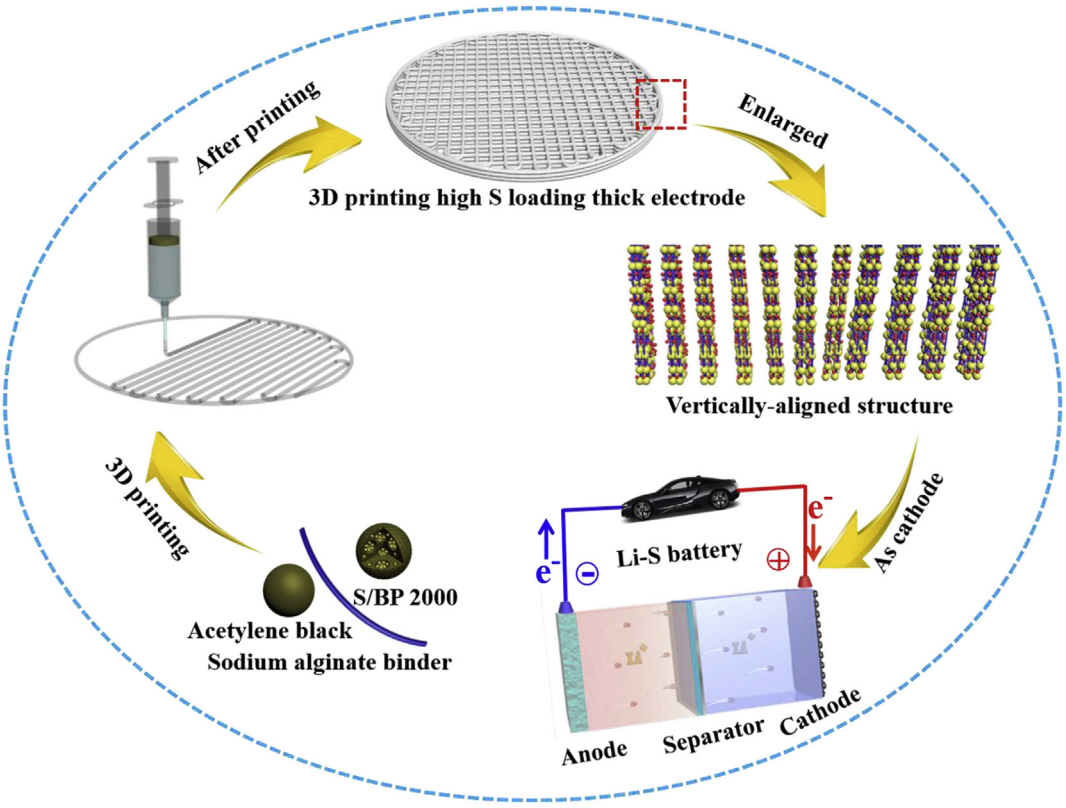

Fig. 1. Schematic illustration of the 3D-printed vertical aligned electrode (3DP-VAE) applied in Li-S batteries.

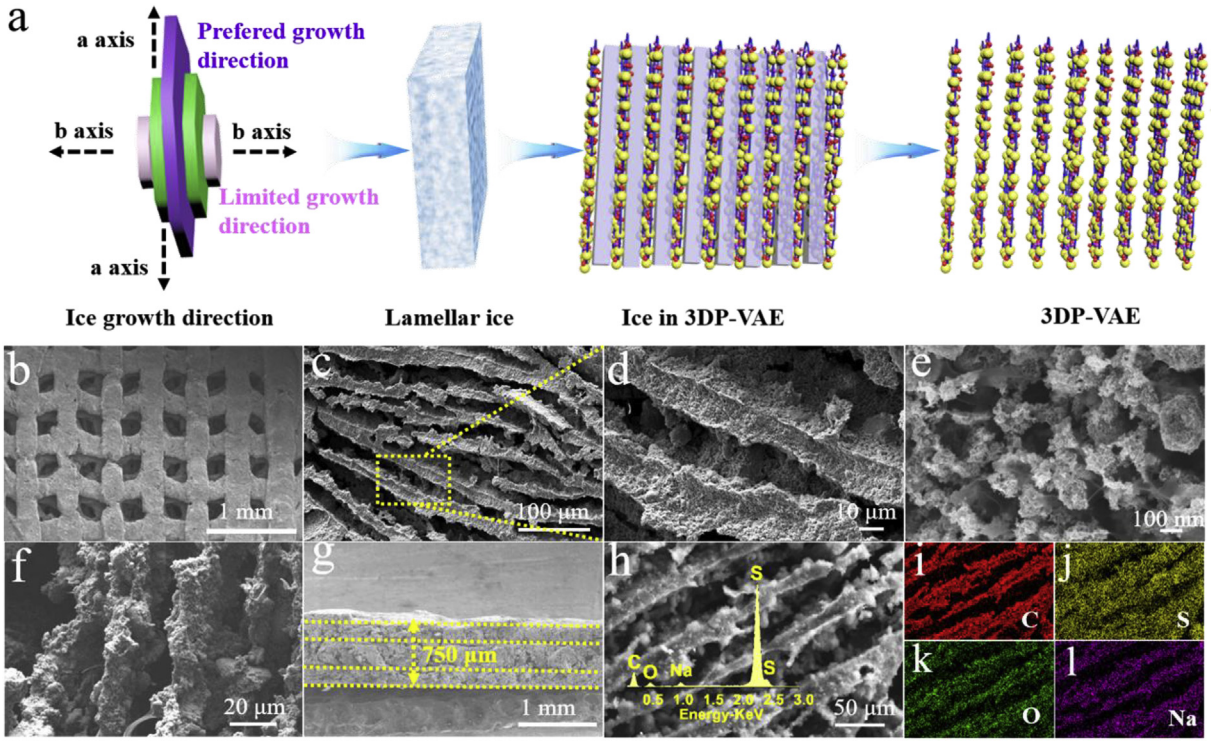

Fig. 2. (a) The mechanism of lamellar growth of ice inside the 3DP-VAE; (b–e) SEM images of 3DP-VAE-6 (750 μm with 6 mg cm^{-2} sulfur) with different magnification; (f–g) cross-sectional SEM images of 3DP-VAE-6 with 3 layers at different magnification; (h) SEM image with an inset of EDX spectrum and (i–l) corresponding elemental mappings of 3DP-VAE-6.

distance between two adjacent fibers was about 250 μm that constructs orderly distributed square pores by design. This provided sufficient Li^+ transport channels and accommodations for electrolyte. In addition to the macroscopic pores created by 3D printing, higher magnification SEM

images in Fig. 2c and d depict the constitution of numerous lamellar electrodes (~20 μm thick). Vertically aligned Li^+ transport channels were constructed in micro-scale. It is widely accepted that the electrochemical reactions can only occur at the tri-phase interface of e^- source, Li^+ source, and active material. In this consideration, each "thin electrode" is favorable for electrochemical reactions. Considering negligible Li^+ transporting resistance in micro-scale channels, the largest Li^+ transport distance is only around 10 μm assuming a bi-directional transport model and ignoring the tortuosity in "thin electrode". The short Li^+ diffusion length is beneficial for reaction kinetics and alleviation of Li_2S_2/Li_2S blockage. Moreover, the "thin electrodes" showed a constant thickness of 20 μm no matter the total thickness of the thick electrodes. The morphology and structure of "thin electrodes" is further clarified by SEM with higher magnification. As shown in Fig. 2e, the nano-sized pores in the "thin electrode" can further accommodate electrolyte and facilitate Li^+ transport. Fig. 2g shows the cross-sectional view of the 3DP-VAE-6 electrode. The 3DP-VAE-6 electrode is composed of 3 printing layers with a thickness of 250 μm for each layer. A magnified cross-sectional view is shown in Fig. 2f. Similar vertically aligned Li^+ transport channels were observed. The morphology of 3DP-VAE-2 (sulfur loading of 2 mg cm^{-2}) electrode with a single printed layer (250 μm) is shown in Fig. S2. The 3DP-VAE-2 electrode was also composed of similar micro-sized "thin electrodes" with a thickness of ~20 μm. The successful formation of "thin electrodes" via ice-template was independent of the total thickness of electrodes. Similar Li^+/e^- conductivities in both 3DP-VAE-2 and 3DP-VAE-6 electrodes and thickness-independent electrochemical performance were expected.

For comparison, some printed electrodes were conventionally dried in a vacuum oven at 60 °C, denoted as 3D-printed none vertical aligned electrode (3DP-NVAEs). As shown in Fig. S3, both the 3DP-NVAEs with sulfur loading of 2 and 6 mg cm^{-2} (3DP-NVAE-2 and 3DP-NVAE-6, respectively) were dense without vertical aligned "thin electrodes". Due to surface tension, the printed grid structure of 3DP-NVAE electrodes is mostly fractured. This can be harmful for Li^+ transport. The sulfur content in the S/BP 2000 composite was determined to be 60 wt% by thermogravimetric analysis (TGA) in N_2 atmosphere (Fig. S4).

Figure S5 shows the cyclic voltammetry (CV) curves of Li-S batteries using 3DP-VAE-6 and 3DP-NVAE-6 electrodes. Both batteries demonstrated two couples of oxidation/reduction peaks in the selected voltage window from 1.8 to 2.8 V. The 3DP-VAE-6 cell exhibited two oxidization peaks at 2.35 and 2.44 V and two reduction peaks at 2.27 and 1.96 V, indicating a two-step oxidation/reduction process between sulfur and the discharge products Li_2S_2/Li_2S. In contrast, the oxidization peaks of the 3DP-NVAE-6 cell shifted to higher voltages of 2.40 and 2.50 V, while the reduction peak shifted to lower voltages of 2.24 and 1.90V. The polarized and broadened oxidation/reduction peaks indicated poorer electrochemical kinetics than the 3DP-VAE-6 cell. The difference between 3DP-VAEs and 3DP-NVAEs was further investigated by the electrochemical impedance spectroscopy (EIS). As shown in Fig. S6a and Table S1, the four electrodes exhibit similar ohmic resistance less than around 8 Ω, while the charge transfer resistance(R_{ct}) were quite different. Noting that R_{ct} is closely related to the chemical reaction activation energy, the similar R_{ct} values of 3DP-VAE-2 (36.62 Ω) and 3DP-VAE-6 (44.51 Ω) suggested their similar electrochemical reaction kinetics. Comparing with the 3DP-VAEs, the 3DP-NVAEs presented larger R_{ct} values (51.64 Ω for the 3DP-NVAE-2 and 83.37 Ω for the 3DP-NVAE-6). Slower electrochemical reaction kinetics of the 3DP-NVAEs than the 3DP-VAEs was indicated, presumably due to the decreased active sites in the dense 3DP-NVAEs. To further quantify the difference of Li^+ diffusion in 3DP-VAEs and 3DP-NVAEs, the diffusion coefficient of Li^+ (D_{Li+}) was calculated based on the D_{Li}^+ Warburg coefficient (σ) and angular frequency (ω) relationship in previous reports [33,34]. As shown in Fig. S6b and Table S1, The 3DP-VAE-2 and 3DP-VAE-6 electrodes exhibit similar D_{Li+} of 2.29×10^{-10} and 1.54×10^{-10} $cm^2 s^{-1}$, which were nearly one order of magnitude higher than that of the 3DP-NVAE-2 and 3DP-NVAE-6 electrodes (2.72×10^{-11} and 1.81×10^{-11} $cm^2 s^{-1}$). The 3DP-VAEs possessed smaller R_{ct} and larger D_{Li+}, suggesting higher electrochemical activity and faster Li^+ diffusion than the 3DP-NVAEs. This emphasized the importance of the unique structure of the 3DP-VAEs.The similar kinetics obtained for 3DP-VAE-2 and 3DP-VAE-6 electrodes with different sulfur loadings indicate the similar electrochemical kinetics and thickness-independent electrochemical performance.

The thickness-independent properties of the 3DP-VAEs were demonstrated by the rate performance and cycling stability. As shown in Fig. 3a, the 3DP-VAE-2 cell delivered average capacities of 854, 820, 798, 775, 719, 644, 641 and 531 mA h g^{-1} at current densities of 1, 2, 3, 4, 5, 6, 8 and 10 mA cm^{-2}, respectively. When the current density returned to 1 mA cm^{-2}, a high specific capacity of 798 mA h g^{-1} was maintained. It is noteworthy that the 3DP-VAE-6 cell demonstrated very similar rate performance as the 3DP-VAE-2 cell at the same current densities from 1 to 10 mA cm^{-2}, which were 885, 804, 764, 750, 734, 714, 649 and 532 mA h g^{-1}, respectively. When the current density was changed back to 1 mA cm^{-2}, a similar discharge capacity of 784.3 mA h g^{-1} was recovered. In great contrast, the rate performance of the 3DP-NVAEs was not at all comparable, with the higher loading 3DP-NVAE-6 failed even more rapidly. When the current density increased to 5 mA cm^{-2}, the 3DP-NVAE-6 delivered almost no capacity. The poor rate performance of the 3DP-NVAEs was mainly attributed to the blocked Li^+/e^- transport in a thick and dense electrode. Fig. 3b shows the charge/discharge profiles for the 3DP-VAEs and 3DP-NVAEs at the first cycle. At a current density of 1 mA cm^{-2}, all four electrodes presented a similar capacity of approximately 1200 mAh g^{-1}. However, it is noteworthy that the overpotential of 3DP-VAEs was smaller than that of the 3DP-NVAEs. Additionally, the polarization of the 3DP-NVAEs was highly dependent on the sulfur loading, but the 3DP-VAEs were relatively independent. A higher sulfur loading in 3DP-NVAEs led to a larger overpotential, while the charge/discharge profiles of the different loading 3DP-VAEs almost overlapped. This again emphasizes the important improvements of Li^+/e^- transport by the built-in "thin electrodes". The thickness-independent performance of 3DP-VAEs was also observed during the rate performance test. The galvanostatic charge/discharge curves of the 3DP-VAE-2 and 3DP-VAE-6 cells at different current densities are shown in Figs. S7a and b. The typical two discharge plateaus for both electrodes can be well observed even at the high current density of 10 mA cm^{-2}, indicating a kinetic effective process. However, both the 3DP-NVAE-2 and 3DP-NVAE-6 lost the second discharge plateau at a current density of 8 mA cm^{-2} and 4 mA cm^{-2} (Fig. S8). The sudden tendency changing of the charge/discharge curves from 6 mA cm^{-2} to 8 mA cm^{-2} in Fig. S8a can be explained as follows. When we increase the current density from 6 mA cm^{-2} to 8 mA cm^{-2}, the overpotential will further increase and the discharge plateau voltage will be lower. As can be seen from Fig. S8, there is an obvious valley between the first plateau and the second plateau, which is called Li_2S nucleation point [35]. Generally, the voltage at the Li_2S nucleation point is much lower compared with both first discharge plateau and second discharge plateau due to the higher internal resistance [35]. At a current density of 6 mA cm^{-2}, the voltage of the Li_2S nucleation point is around 1.85 V, closing to the cutoff voltage of 1.8 V. When overpotential further increasing at a current density of 8 mA cm^{-2}, the voltage of the Li_2S nucleation point will be lower than 1.8 V, thus resulting in discharge termination and disappearance of second discharge plateau. The severe polarization upon increasing current density was common for conventional dense thick electrodes. Moreover, the overpotential (ΔV), determined by the charge/discharge voltage difference at the median value of the discharge capacity, of those four electrodes at various current densities from 2 to 10 mA cm^{-2} were calculated and compared in Fig. 3c. The ΔV values of the 3DP-VAE-2 cell at 2, 4, 6 and 8 mA cm^{-2} were 198, 275, 332 and 391 mV, respectively. Interestingly, the 3DP-VAE-6 cell showed almost the same ΔV values of 219, 290, 365 and 423 mV at the corresponding current densities. Even at a high current density of 10 mA cm^{-2}, the 3DP-VAE-2 and 3DP-VAE-6 cells still exhibited similar ΔV values of 455 and 465 mV, respectively. The 3DP-VAEs were proved to have similar Li^+/e^- transport

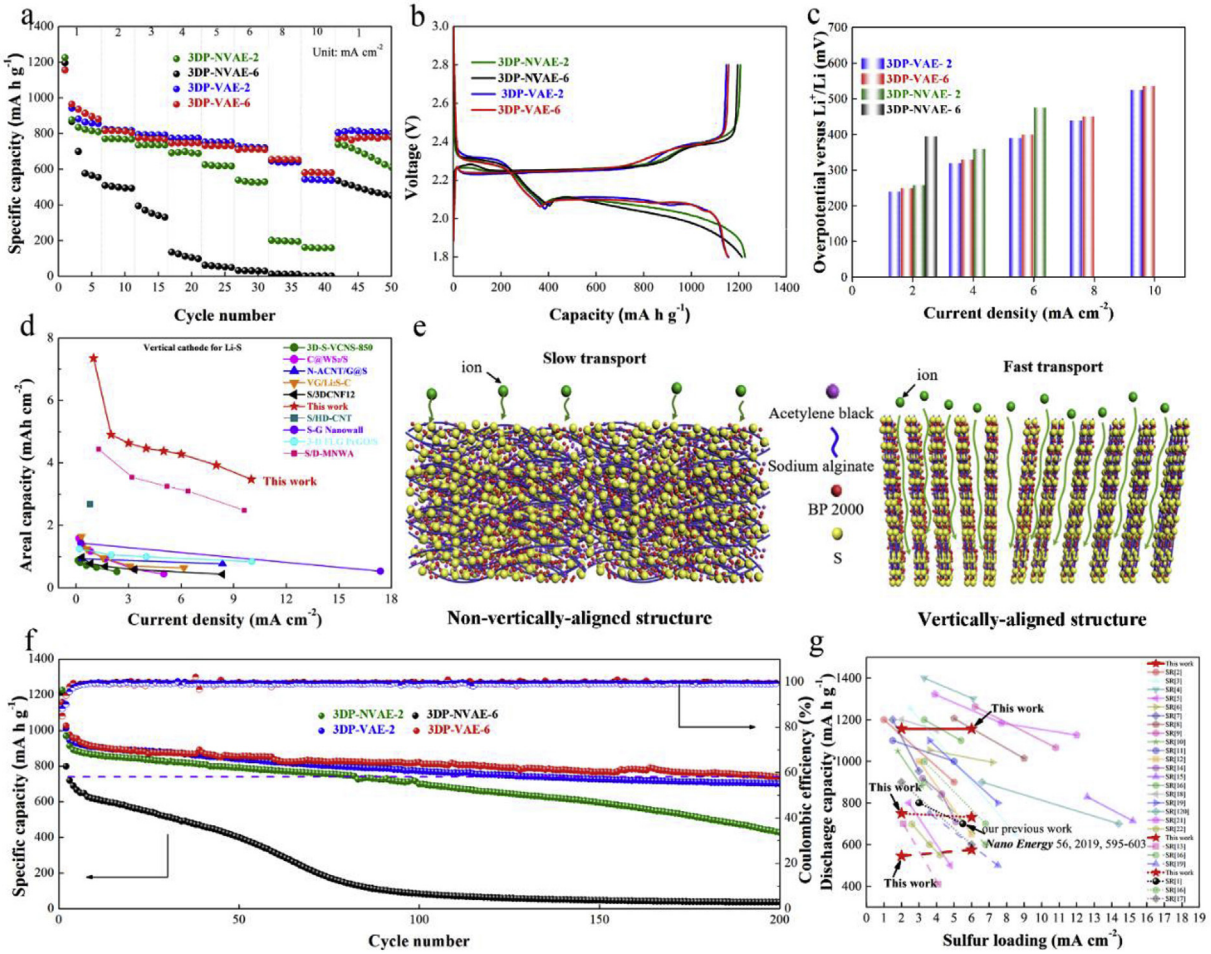

Fig. 3. Comparison on electrochemical performance of Li-S batteries using 3DP-VAEs and 3DP-NVAEs with different sulfur loadings. (a) Rate performance of 3DP-VAEs and 3DP-NVAEs with different sulfur loadings at various current rates from 1 to 10 mA cm^{-2}. (b) Initial charge and discharge curves of 3DP-VAEs and 3DP-NVAEs with different sulfur loadings at current density of 1 mA cm^{-2}. (c) Overpotentials of 3DP-VAEs and 3DP-NVAEs various rates. (d) Ragone plot comparing areal capacity versus current density for the 3DP-VAE-6 to the reported vertical electrodes for Li-S batteries. (e) Schematic illustration of ion transport in 3DP- NVAE-6 and 3DP-VAE-6; the green arrowed curves indicate ionic pathways. (f) Cycling performance of 3DP-VAEs and 3DP-NVAEs with different sulfur loadings at a current density of 1 mA cm^{-2}. (g) Comparison of the recently reported discharge capacities with different sulfur loadings, corresponding with Table S2 (solid line: around 1 mA cm^{-2}; dash dot: around 5 mA cm^{-2}; dash line: around 10 mA cm^{-2}). (For interpretation of the references to colour in this figure legend, the reader is referred to the Web version of this article.)

capabilities and thus thickness-independent electrochemical performance. In contrast, for 3DP-NVAEs, the ΔV dramatically increased with the increasing thickness and sulfur loading of the electrode, consistent with the common trend of most recently reported Li-S batteries [36,37]. The 3DP-NVAE-6 presented the largest ΔV value among the four electrodes, almost two times higher than those of the 3DP-VAEs at 2 mA cm^{-2}. The ΔV values of 3DP-NVAE-2 and 3DP-NVAE-6 are not shown in Fig. 3c beyond current densities of 6 mA cm^{-2} and 2 mA cm^{-2} due to the absence of the second discharge plateau. The Ragone plot in Future 3d compares the performance of the 3DP-VAE-6 to the reported vertical-aligned cathodes for Li-S batteries during the years between 2014 and 2018 [27,28,38–44]. The areal capacity of our 3DP-VAE-6 substantially exceeds other reported vertical-aligned cathodes for Li-S batteries at the same current densities. The improved rate performance and decreased overpotential of 3DP-VAE electrodes are attributed to the improved electrochemical kinetics and fast Li^+/e^- transport in the "thin electrodes". As schematically illustrated in Fig. 3e, the Li^+ can first diffuse into the micro-scale vertical-aligned Li^+ transport channels with negligible transport resistance, then transport in the porous "thin electrodes" bi-directionally. The longest Li^+ transport distance is presumably only half of the thickness of the "thin electrodes" (~10 μm). In contrast, Li^+ has to diffuse a long distance in the dense 3DP-NVAEs for full sulfur utilization, which often cannot complete at high current densities. Therefore, the thickness-independent rate performance of 3DP-VAEs is a particular advantage over conventional electrodes for achieving effective and high sulfur loading.

The cycling stability of those four cathodes was evaluated at 1 mA cm^{-2}. As shown in Fig. 3f, the 3DP-VAE-2 and 3DP-VAE-6 cells delivered initial capacities of 1157.2 mA h g^{-1} and 1156.4 mA h g^{-1} and reversible capacities of 906.6 mA h g^{-1} and 910.3 mA h g^{-1} after 10 cycles of stabilization, respectively. The capacity decays in the first cycle to the 10th cycles, which is mainly attributed to some polysulfides will be remained in the electrolyte and can't be utilized. After the polysulfides concentration in the electrolyte is equal to the ones in the cathode materials, negligible polysulfides diffuse into the electrolyte and a kinetic balance is achieved. So after decay in a few cycles, a reversible and stable capacity will be achieved [12]. After 200 cycles, high discharge capacities of 701.3 mA h g^{-1} and 739.6 mA h g^{-1} were retained for 3DP-VAE-2 and 3DP-VAE-6, demonstrating a low capacity attenuation of around 0.10% per cycle (calculated based on the stabilized capacities at the 10th cycle) for both electrodes. The excellent cycling performance indicated well confinement of PSs in the 3DP-VAEs, either in the vertically aligned channels or the nano-scale pores in the "thin electrodes"; the fast reaction kinetics thanks to the unique electrode structural design also reduced the

active materials loss during repeated charge/discharge process. In contrast, although the 3DP-NVAE cells showed high initial capacities above 1200 mA h g^{-1}, the reversible capacities dropped to 863.8 mA h g^{-1} and even 616.0 mA h g^{-1} at the 10th cycle for 3DP-NVAE-2 and 3DP-NVAE-6, respectively. After 200 cycles, capacities of only 428.2 mA h g^{-1} and 36.6 mA h g^{-1} were maintained for the 3DP-NVAE-2 and 3DP-NVAE-6 cells, corresponding to high capacity attenuations of 0.27% and 0.49%, respectively [45,46]. The poor cycling stability of 3DP-NVAEs could mainly be attributed to the high concentration of Li_2S deposited on the surface of 3DP-NVAEs and blocked the Li^+/e^- pathways. The areal capacities achieved by 3DP-VAEs and 3DP-NVAEs cells were shown in Fig. S9. The 3DP-VAE-2 and 3DP-VAE-6 cells delivered initial areal capacities of 2.31 and 6.94 mA h cm^{-2} and maintained at 1.40 and 4.44 mA h cm^{-2} even after 200 cycles, respectively, which were higher than that of 3DP-NVAEs cells. Remarkably, the evaluation of discharge capacity followed by increasing the sulfur loading from recently publications was presented in Fig. 3g and listed in Table S2. As expected, due to the worsening Li^+/e^- transport with sulfur loading increasing, the capacities are decreased gradually, which will no doubt limit the improvement of practical energy density. In contrast, as shown in Fig. 3g marked with red pentagrams, beneficial from the thickness-independent property enabled by the vertically-aligned structure, there is no capacity drop for the 3DP-VAEs with sulfur loading increasing, even at high current density of 10 mA cm^{-2}, further highlighting the novel thickness-independent structure in Li-S batteries.

As shown in Fig. 4a and Fig. 4b, the electrochemical reactions can only occur at the tri-phase interface of the electrolyte (Li^+ source), cathode active site (e^- source) and active materials; the transformation from a thick dense electrode into numerous vertically aligned "thin electrodes" substantially enhanced the number of tri-phase interfaces and facilitated conversion between sulfur and Li_2S_2/Li_2S. The sturdiness of the designed structure is essential for long-term cycle ability. To examine the structural stability of the 3DP-VAEs over electrochemical operations, the 3DP-VAE-2 and 3DP-VAE-6 cells were disassembled for morphological analysis by SEM after cycling at 2 mA cm^{-2} for 100 cycles. As shown in Fig. 4c and d, both 3DP-VAEs still well maintained the vertically aligned "thin electrodes" for fast local Li^+/e^- transport. No obvious accumulation of reaction side products or "dead" Li_2S_2/Li_2S were observed, especially when compared with 3DP-NVAEs as shown in Fig. S10 which have been cracked during cycling. Moreover, as shown in Fig. S11, EIS curves of 3DP-VAE-2 and 3DP-VAE-6 after cycling also demonstrate a similar electrochemical activity and Li+/e− diffusion capability. Therefore the unique structure of 3DP-VAEs remained effective upon repeated charge/discharge cycles.

4. Conclusions

In summary, we have developed a new strategy to apply 3D printing technique to carry out thickness-independent Li-S cathode by converting the thick electrodes into a combination of numerous vertically aligned "thin electrodes". The "thin electrodes" presented a constant thickness of ~20 μm in spite of the total thickness of the whole electrode. Due to the similar electrochemical kinetics and Li^+/e^- transport distance in "thin electrodes", the prepared 3DP-VAE-2 (250 μm with a sulfur loading of 2 mg cm^{-2}) and 3DP-VAE-6 (750 μm with 6 mg cm^{-2} sulfur) electrodes delivered highly similar cycling performance and rate performance. Both 3DP-VAEs were able to deliver a capacity of 530 mAh g^{-1} at 10 mA cm^{-2} and a low capacity decay of 0.1% per cycle over 200 cycles at 1 mA cm^{-2}. This work opens a new opportunity for designing high-performance and high-energy Li-S batteries with high sulfur loadings.

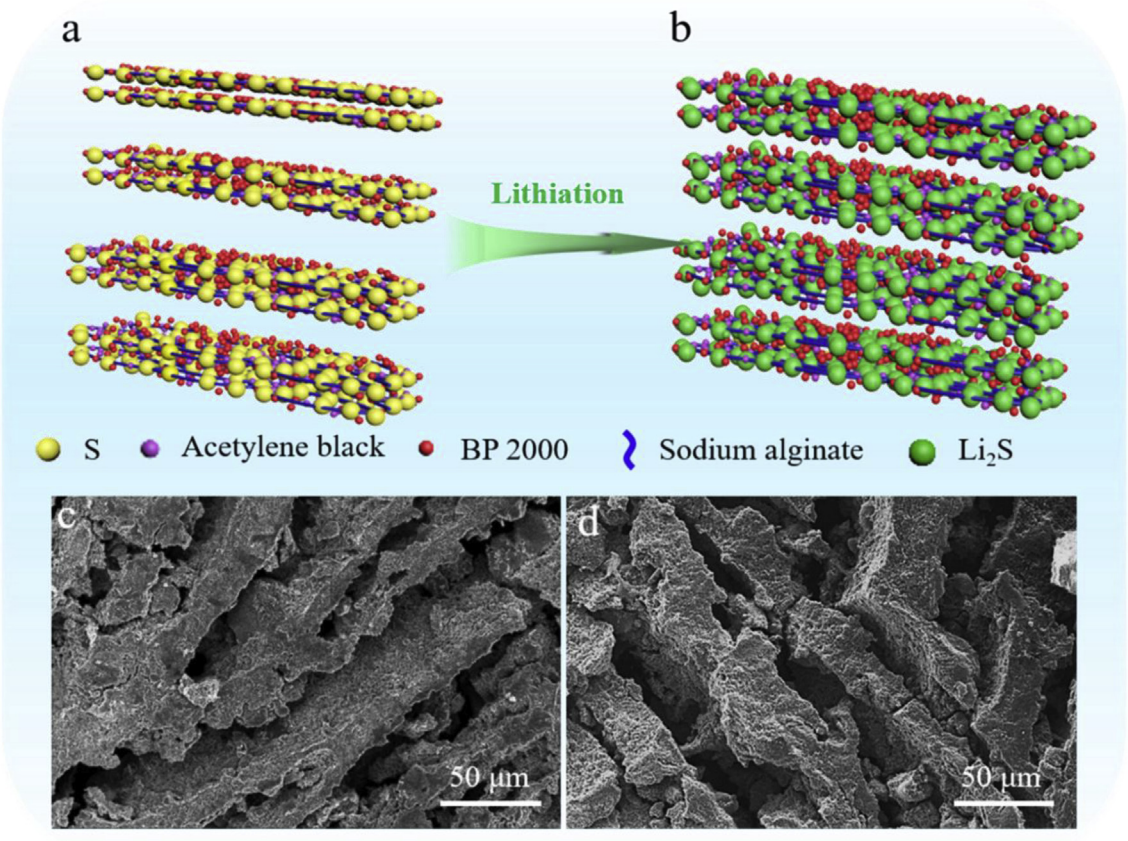

Fig. 4. Schematic diagram of the 3DP-VAE during lithiation process (a, b); comparison of surface morphologies of 3DP-VAE-2 (c) and 3DP-VAE-6 (d) after 100 cycles at 2 mA cm^{-2}.

Author contribution

Xuejie Gao and Xiaofei Yang contributed equally to this work. They conceived the idea and designed the experiments. Xueliang Sun and Tsun-Kong Sham as supervisors gave guidance and discussion to the project. Qian Sun helped design and discussed the experiments. Ruying Li assisted with characterizations. Xuejie Gao, Jing Luo and Jianneng Liang did the Scanning Electron Microscope (SEM) and Thermogravimetric Analysis (TGA) characterization. Xuejie Gao, Weihan Li and Jiwei Wang designed the 3D printing process during printing electrodes. Sizhe Wang and Minsi Li assisted with analyzing CV curves and EIS curves, respectively. Xuejie Gao wrote the manuscript. All authors discussed the results and commented on the manuscript.

Acknowledgements

This research was supported by the Natural Science and Engineering Research Council of Canada (NSERC), the Canada Research Chair Program (CRC), the Canada Foundation for Innovation (CFI), and Western University.

Appendix A. Supplementary data

Supplementary data to this article can be found online at https://doi.org/10.1016/j.ensm.2019.08.001.

References

[1] Q. Pang, X. Liang, C.Y. Kwok, L.F. Nazar, Nat. Energy 1 (2016) 16132.
[2] X. Ji, K.T. Lee, L.F. Nazar, Nat. Mater. 8 (2009) 500–506.
[3] L. Luo, S.-H. Chung, A. Manthiram, Adv. Energy Mater. 8 (2018) 1801014.
[4] X. Li, X. Sun, Adv. Funct. Mater. 28 (2018) 1801323.
[5] X. Li, M. Banis, A. Lushington, X. Yang, Q. Sun, Y. Zhao, C. Liu, Q. Li, B. Wang, W. Xiao, C. Wang, M. Li, J. Liang, R. Li, Y. Hu, L. Goncharova, H. Zhang, T.K. Sham, X. Sun, Nat. Commun. 9 (2018) 4509.
[6] X. Ji, K.T. Lee, L.F. Nazar, Nat. Mater. 8 (2009) 500.
[7] X. Li, A. Lushington, Q. Sun, W. Xiao, J. Liu, B. Wang, Y. Ye, K. Nie, Y. Hu, Q. Xiao, R. Li, J. Guo, T.K. Sham, X. Sun, Nano Lett. 16 (2016) 3545–3549.
[8] X. Yang, N. Yan, W. Zhou, H. Zhang, X. Li, H. Zhang, J. Mater. Chem. A 3 (2015) 15314–15323.
[9] X. Yang, H. Zhang, Y. Chen, Y. Yu, X. Li, H. Zhang, Nano Energy 39 (2017) 418–428.
[10] J. Luo, R.C. Lee, J.T. Jin, Y.T. Weng, C.C. Fang, N.L. Wu, Chem. Commun. 53 (2017) 963–966.
[11] G. Hu, C. Xu, Z. Sun, S. Wang, H.M. Cheng, F. Li, W. Ren, Adv. Mater. 28 (2016) 1603–1609.
[12] X. Gao, X. Yang, M. Li, Q. Sun, J. Liang, J. Luo, J. Wang, W. Li, J. Liang, Y. Liu, S. Wang, Y. Hu, Q. Xiao, R. Li, T.-K. Sham, X. Sun, Adv. Funct. Mater. 29 (2019) 1806724.
[13] H.J. Peng, J.Q. Huang, Q. Zhang, Chem. Soc. Rev. 46 (2017) 5237–5288.
[14] S. Niu, W. Lv, G. Zhou, H. Shi, X. Qin, C. Zheng, T. Zhou, C. Luo, Y. Deng, B. Li, F. Kang, Q.-H. Yang, Nano Energy 30 (2016) 138–145.
[15] X. Yang, X. Li, K. Adair, H. Zhang, X. Sun, Electrochem. Energy Rev. 1 (2018) 239–293.
[16] L. Miao, W. Wang, K. Yuan, Y. Yang, A. Wang, Chem. Commun. 50 (2014) 13231–13234.
[17] B. Anasori, M.R. Lukatskaya, Y. Gogotsi, Nat. Rev. Mater. 2 (2017) 16098.
[18] M.R. Lukatskaya, B. Dunn, Y. Gogotsi, Nat. Commun. 7 (2016) 12647.
[19] S.-E. Cheon, K.-S. Ko, J.-H. Cho, S.-W. Kim, E.-Y. Chin, H.-T. Kim, J. Electrochem. Soc. 150 (2003) A800.
[20] K.H. Wujcik, D.R. Wang, T.A. Pascal, D. Prendergast, N.P. Balsara, J. Electrochem. Soc. 164 (2016) A18–A27.
[21] X. Yang, Y. Chen, M. Wang, H. Zhang, X. Li, H. Zhang, Adv. Funct. Mater. 26 (2016) 8427–8434.
[22] J. Gou, H. Zhang, X. Yang, Y. Chen, Y. Yu, X. Li, H. Zhang, Adv. Funct. Mater. 28 (2018) 1707272.
[23] H. Sun, J. Liang, Z. Zhao, C. Lee, H. Fei, M. Ding, J. Lau, M. Li, C. Wang, X. Xu, G. Hao, B. Papandrea, I. Shakir, B. Dunn, Y. Huang, X. Duan, Science 356 (2017) 599–604.
[24] M.R. Lukatskaya, O. Mashtalir, C.E. Ren, Y. Dall'Agnese, P. Rozier, P.L. Taberna, M. Naguib, P. Simon, M.W. Barsoum, Y. Gogotsi, Science 341 (2013) 15021505.
[25] X. Gao, Q. Sun, X. Yang, J. Liang, A. Koo, W. Li, J. Liang, J. Wang, R. Li, F.B. Holness, A.D. Price, S. Yang, T.-K. Sham, X. Sun, Nano Energy 56 (2019) 595–603.
[26] Y. Xia, T.S. Mathis, M.Q. Zhao, B. Anasori, A. Dang, Z. Zhou, H. Cho, Y. Gogotsi, S. Yang, Nature 557 (2018) 409–412.
[27] B. Li, S. Li, J. Liu, B. Wang, S. Yang, Nano Lett. 15 (2015) 3073–3079.
[28] S. Rehman, X. Gu, K. Khan, N. Mahmood, W. Yang, X. Huang, S. Guo, Y. Hou, Adv. Energy Mater. 6 (2016) 1502518.
[29] J. Billaud, F. Bouville, T. Magrini, C. Villevieille, A.R. Studart, Nat. Energy 1 (2016) 16097.
[30] J. Wang, Q. Sun, X. Gao, C. Wang, W. Li, F.B. Holness, M. Zheng, R. Li, A.D. Price, X. Sun, T.K. Sham, X. Sun, ACS Appl. Mater. Inter. 10 (2018) 39794–39801.
[31] Q. Cheng, C. Huang, A.P. Tomsia, Adv. Mater. 29 (2017) 1703155.
[32] S. Deville, Adv. Eng. Mater. 10 (2008) 155–169.
[33] X. Yang, Y. Yu, N. Yan, H. Zhang, X. Li, H. Zhang, J. Mater. Chem. A 4 (2016) 5965–5972.
[34] Y. Cheng, K. Feng, W. Zhou, H. Zhang, X. Li, H. Zhang, Dalton Trans. 44 (2015) 17579–17586.
[35] J. Park, E.T. Kim, C. Kim, J. Pyun, H.-S. Jang, J. Shin, J.W. Choi, K. Char, Y.-E. Sung, Adv. Energy Mater. 7 (2017) 1700074.
[36] M.K. Song, E.J. Cairns, Y. Zhang, Nanoscale 5 (2013) 2186–2204.
[37] X. Liang, C. Hart, Q. Pang, A. Garsuch, T. Weiss, L.F. Nazar, Nat. Commun. 6 (2015) 5682.
[38] T. Lei, W. Chen, J. Huang, C. Yan, H. Sun, C. Wang, W. Zhang, Y. Li, J. Xiong, Adv. Energy Mater. 7 (2017) 1601843.
[39] C. Tang, Q. Zhang, M.Q. Zhao, J.Q. Huang, X.B. Cheng, G.L. Tian, H.J. Peng, F. Wei, Adv. Mater. 26 (2014) 6100–6105.
[40] D. Wang, X. Xia, Y. Wang, D. Xie, Y. Zhong, J. Wu, X. Wang, J. Tu, Chemistry 23 (2017) 11169–11174.
[41] S. Feng, J. Song, S. Fu, C. Zhu, Q. Shi, M.-K. Song, D. Du, Y. Lin, J. Mater. Chem. A 5 (2017) 23737–23743.
[42] K. Xi, B. Chen, H. Li, R. Xie, C. Gao, C. Zhang, R.V. Kumar, J. Robertson, Nano Energy 12 (2015) 538–546.
[43] D.P. Singh, N. Soin, S. Sharma, S. Basak, S. Sachdeva, S.S. Roy, H.W. Zanderbergen, J.A. McLaughlin, M. Huijben, M. Wagemaker, Sustain. Energy Fuels 1 (2017) 1516–1523.
[44] X. Yang, Y. Yu, X. Lin, J. Liang, K. Adair, Y. Zhao, C. Wang, X. Li, Q. Sun, H. Zhang, X. Li, R. Li, Zhang Huamin, X. Sun, J. Mater. Chem. A 6 (2018) 22958–22965.
[45] Y. Yan, M. Shi, Y. Wei, C. Zhao, M. Carnie, R. Yang, Y. Xu, J. Alloy. Comp. 738 (2018) 16–24.
[46] D.-R. Deng, T.-H. An, Y.-J. Li, Q.-H. Wu, M.-S. Zheng, Q.-F. Dong, J. Mater. Chem. A 4 (2016) 16184–16190.